

Measurement of the ϕ_η^* distribution of muon pairs with masses between 30 and 500 GeV in 10.4 fb^{-1} of $p\bar{p}$ collisions

V.M. Abazov,³¹ B. Abbott,⁶⁷ B.S. Acharya,²⁵ M. Adams,⁴⁶ T. Adams,⁴⁴ J.P. Agnew,⁴¹ G.D. Alexeev,³¹ G. Alkhazov,³⁵ A. Alton^a,⁵⁶ A. Askew,⁴⁴ S. Atkins,⁵⁴ K. Augsten,⁷ C. Avila,⁵ F. Badaud,¹⁰ L. Bagby,⁴⁵ B. Baldin,⁴⁵ D.V. Bandurin,⁷³ S. Banerjee,²⁵ E. Barberis,⁵⁵ P. Baringer,⁵³ J.F. Bartlett,⁴⁵ U. Bassler,¹⁵ V. Bazterra,⁴⁶ A. Bean,⁵³ M. Begalli,² L. Bellantoni,⁴⁵ S.B. Beri,²³ G. Bernardi,¹⁴ R. Bernhard,¹⁹ I. Bertram,³⁹ M. Besançon,¹⁵ R. Beuselinck,⁴⁰ P.C. Bhat,⁴⁵ S. Bhatia,⁵⁸ V. Bhatnagar,²³ G. Blazey,⁴⁷ S. Blessing,⁴⁴ K. Bloom,⁵⁹ A. Boehnlein,⁴⁵ D. Boline,⁶⁴ E.E. Boos,³³ G. Borissoy,³⁹ M. Borysova^l,³⁸ A. Brandt,⁷⁰ O. Brandt,²⁰ R. Brock,⁵⁷ A. Bross,⁴⁵ D. Brown,¹⁴ X.B. Bu,⁴⁵ M. Buehler,⁴⁵ V. Buescher,²¹ V. Bunichev,³³ S. Burdin^b,³⁹ C.P. Buszello,³⁷ E. Camacho-Pérez,²⁸ B.C.K. Casey,⁴⁵ H. Castilla-Valdez,²⁸ S. Caughron,⁵⁷ S. Chakrabarti,⁶⁴ K.M. Chan,⁵¹ A. Chandra,⁷² E. Chapon,¹⁵ G. Chen,⁵³ S.W. Cho,²⁷ S. Choi,²⁷ B. Choudhary,²⁴ S. Cihangir,⁴⁵ D. Claes,⁵⁹ J. Clutter,⁵³ M. Cooke^k,⁴⁵ W.E. Cooper,⁴⁵ M. Corcoran,⁷² F. Couderc,¹⁵ M.-C. Cousinou,¹² D. Cutts,⁶⁹ A. Das,⁴² G. Davies,⁴⁰ S.J. de Jong,^{29,30} E. De La Cruz-Burelo,²⁸ F. Déliot,¹⁵ R. Demina,⁶³ D. Denisov,⁴⁵ S.P. Denisov,³⁴ S. Desai,⁴⁵ C. Deterre^c,⁴¹ K. DeVaughan,⁵⁹ H.T. Diehl,⁴⁵ M. Diesburg,⁴⁵ P.F. Ding,⁴¹ A. Dominguez,⁵⁹ A. Dubey,²⁴ L.V. Dudko,³³ A. Duperrin,¹² S. Dutt,²³ M. Eads,⁴⁷ D. Edmunds,⁵⁷ J. Ellison,⁴³ V.D. Elvira,⁴⁵ Y. Enari,¹⁴ H. Evans,⁴⁹ V.N. Evdokimov,³⁴ A. Fauré,¹⁵ L. Feng,⁴⁷ T. Ferbel,⁶³ F. Fiedler,²¹ F. Filthaut,^{29,30} W. Fisher,⁵⁷ H.E. Fisk,⁴⁵ M. Fortner,⁴⁷ H. Fox,³⁹ S. Fuess,⁴⁵ P.H. Garbincius,⁴⁵ A. Garcia-Bellido,⁶³ J.A. García-González,²⁸ V. Gavrilov,³² W. Geng,^{12,57} C.E. Gerber,⁴⁶ Y. Gershtein,⁶⁰ G. Ginther,^{45,63} O. Gogota,³⁸ G. Golovanov,³¹ P.D. Grannis,⁶⁴ S. Greder,¹⁶ H. Greenlee,⁴⁵ G. Grenier,¹⁷ Ph. Gris,¹⁰ J.-F. Grivaz,¹³ A. Grohsjean^c,¹⁵ S. Grünendahl,⁴⁵ M.W. Grünewald,²⁶ T. Guillemin,¹³ G. Gutierrez,⁴⁵ P. Gutierrez,⁶⁷ J. Haley,⁶⁸ L. Han,⁴ K. Harder,⁴¹ A. Harel,⁶³ J.M. Hauptman,⁵² J. Hays,⁴⁰ T. Head,⁴¹ T. Hebbeker,¹⁸ D. Hedin,⁴⁷ H. Hegab,⁶⁸ A.P. Heinson,⁴³ U. Heintz,⁶⁹ C. Hensel,¹ I. Heredia-De La Cruz^d,²⁸ K. Herner,⁴⁵ G. Hesketh^f,⁴¹ M.D. Hildreth,⁵¹ R. Hirosky,⁷³ T. Hoang,⁴⁴ J.D. Hobbs,⁶⁴ B. Hoeneisen,⁹ J. Hogan,⁷² M. Hohlfeld,²¹ J.L. Holzbauer,⁵⁸ I. Howley,⁷⁰ Z. Hubacek,^{7,15} V. Hynek,⁷ I. Iashvili,⁶² Y. Ilchenko,⁷¹ R. Illingworth,⁴⁵ A.S. Ito,⁴⁵ S. Jabeen^m,⁴⁵ M. Jaffré,¹³ A. Jayasinghe,⁶⁷ M.S. Jeong,²⁷ R. Jesik,⁴⁰ P. Jiang,⁴ K. Johns,⁴² E. Johnson,⁵⁷ M. Johnson,⁴⁵ A. Jonckheere,⁴⁵ P. Jonsson,⁴⁰ J. Joshi,⁴³ A.W. Jung,⁴⁵ A. Juste,³⁶ E. Kajfasz,¹² D. Karmanov,³³ I. Katsanos,⁵⁹ M. Kaur,²³ R. Kehoe,⁷¹ S. Kermiche,¹² N. Khalatyan,⁴⁵ A. Khanov,⁶⁸ A. Kharchilava,⁶² Y.N. Kharzheev,³¹ I. Kiselevich,³² J.M. Kohli,²³ A.V. Kozelov,³⁴ J. Kraus,⁵⁸ A. Kumar,⁶² A. Kupco,⁸ T. Kurča,¹⁷ V.A. Kuzmin,³³ S. Lammers,⁴⁹ P. Lebrun,¹⁷ H.S. Lee,²⁷ S.W. Lee,⁵² W.M. Lee,⁴⁵ X. Lei,⁴² J. Lellouch,¹⁴ D. Li,¹⁴ H. Li,⁷³ L. Li,⁴³ Q.Z. Li,⁴⁵ X. Li,⁴¹ J.K. Lim,²⁷ D. Lincoln,⁴⁵ J. Linnemann,⁵⁷ V.V. Lipaev,³⁴ R. Lipton,⁴⁵ H. Liu,⁷¹ Y. Liu,⁴ A. Lobodenko,³⁵ M. Lokajicek,⁸ R. Lopes de Sa,⁴⁵ R. Luna-Garcia^g,²⁸ A.L. Lyon,⁴⁵ A.K.A. Maciel,¹ R. Madar,¹⁹ R. Magaña-Villalba,²⁸ S. Malik,⁵⁹ V.L. Malyshev,³¹ J. Mansour,²⁰ J. Martínez-Ortega,²⁸ R. McCarthy,⁶⁴ C.L. McGivern,⁴¹ M.M. Meijer,^{29,30} A. Melnitchouk,⁴⁵ D. Menezes,⁴⁷ P.G. Mercadante,³ M. Merkin,³³ A. Meyer,¹⁸ J. Meyerⁱ,²⁰ F. Miconi,¹⁶ N.K. Mondal,²⁵ M. Mulhearn,⁷³ E. Nagy,¹² M. Narain,⁶⁹ R. Nayyar,⁴² H.A. Neal,⁵⁶ J.P. Negret,⁵ P. Neustroev,³⁵ H.T. Nguyen,⁷³ T. Nunnemann,²² J. Orduna,⁷² N. Osman,¹² J. Osta,⁵¹ A. Pal,⁷⁰ N. Parashar,⁵⁰ V. Parihar,⁶⁹ S.K. Park,²⁷ R. Partridge^e,⁶⁹ N. Parua,⁴⁹ A. Patwa^j,⁶⁵ B. Penning,⁴⁵ M. Perfilov,³³ Y. Peters,⁴¹ K. Petridis,⁴¹ G. Petrillo,⁶³ P. Pétrouff,¹³ M.-A. Pleier,⁶⁵ V.M. Podstavkov,⁴⁵ A.V. Popov,³⁴ M. Prewitt,⁷² D. Price,⁴¹ N. Prokopenko,³⁴ J. Qian,⁵⁶ Y. Qin,⁴¹ A. Quadt,²⁰ B. Quinn,⁵⁸ P.N. Ratoff,³⁹ I. Razumov,³⁴ I. Ripp-Baudot,¹⁶ F. Rizatdinova,⁶⁸ M. Rominsky,⁴⁵ A. Ross,³⁹ C. Royon,¹⁵ P. Rubinov,⁴⁵ R. Ruchti,⁵¹ G. Sajot,¹¹ A. Sánchez-Hernández,²⁸ M.P. Sanders,²² A.S. Santos^h,¹ G. Savage,⁴⁵ M. Savitskiy,³⁸ L. Sawyer,⁵⁴ T. Scanlon,⁴⁰ R.D. Schamberger,⁶⁴ Y. Scheglov,³⁵ H. Schellman,⁴⁸ C. Schwanenberger,⁴¹ R. Schwienhorst,⁵⁷ J. Sekaric,⁵³ H. Severini,⁶⁷ E. Shabalina,²⁰ V. Shary,¹⁵ S. Shaw,⁴¹ A.A. Shchukin,³⁴ V. Simak,⁷ P. Skubic,⁶⁷ P. Slattery,⁶³ D. Smirnov,⁵¹ G.R. Snow,⁵⁹ J. Snow,⁶⁶ S. Snyder,⁶⁵ S. Söldner-Rembold,⁴¹ L. Sonnenschein,¹⁸ K. Soustruznik,⁶ J. Stark,¹¹ D.A. Stoyanova,³⁴ M. Strauss,⁶⁷ L. Suter,⁴¹ P. Svoisky,⁶⁷ M. Titov,¹⁵ V.V. Tokmenin,³¹ Y.-T. Tsai,⁶³ D. Tsybychev,⁶⁴ B. Tuchming,¹⁵ C. Tully,⁶¹ L. Uvarov,³⁵ S. Uvarov,³⁵ S. Uzunyan,⁴⁷ R. Van Kooten,⁴⁹ W.M. van Leeuwen,²⁹ N. Varelas,⁴⁶ E.W. Varnes,⁴² I.A. Vasilyev,³⁴ A.Y. Verkhnev,³¹ L.S. Vertogradov,³¹ M. Verzocchi,⁴⁵ M. Vesterinen,⁴¹ D. Vilanova,¹⁵ P. Vokac,⁷ H.D. Wahl,⁴⁴ M.H.L.S. Wang,⁴⁵ J. Warchol,⁵¹ G. Watts,⁷⁴ M. Wayne,⁵¹ J. Weichert,²¹ L. Welty-Rieger,⁴⁸

M.R.J. Williams^{n, 49} G.W. Wilson,⁵³ M. Wobisch,⁵⁴ D.R. Wood,⁵⁵ T.R. Wyatt,⁴¹ Y. Xie,⁴⁵ R. Yamada,⁴⁵ S. Yang,⁴ T. Yasuda,⁴⁵ Y.A. Yatsunencko,³¹ W. Ye,⁶⁴ Z. Ye,⁴⁵ H. Yin,⁴⁵ K. Yip,⁶⁵ S.W. Youn,⁴⁵ J.M. Yu,⁵⁶ J. Zennamo,⁶² T.G. Zhao,⁴¹ B. Zhou,⁵⁶ J. Zhu,⁵⁶ M. Zielinski,⁶³ D. Ziemska,⁴⁹ and L. Zivkovic¹⁴

(The D0 Collaboration*)

¹LAFEX, Centro Brasileiro de Pesquisas Físicas, Rio de Janeiro, Brazil

²Universidade do Estado do Rio de Janeiro, Rio de Janeiro, Brazil

³Universidade Federal do ABC, Santo André, Brazil

⁴University of Science and Technology of China, Hefei, People's Republic of China

⁵Universidad de los Andes, Bogotá, Colombia

⁶Charles University, Faculty of Mathematics and Physics,
Center for Particle Physics, Prague, Czech Republic

⁷Czech Technical University in Prague, Prague, Czech Republic

⁸Institute of Physics, Academy of Sciences of the Czech Republic, Prague, Czech Republic

⁹Universidad San Francisco de Quito, Quito, Ecuador

¹⁰LPC, Université Blaise Pascal, CNRS/IN2P3, Clermont, France

¹¹LPSC, Université Joseph Fourier Grenoble 1, CNRS/IN2P3,
Institut National Polytechnique de Grenoble, Grenoble, France

¹²CPPM, Aix-Marseille Université, CNRS/IN2P3, Marseille, France

¹³LAL, Université Paris-Sud, CNRS/IN2P3, Orsay, France

¹⁴LPNHE, Universités Paris VI and VII, CNRS/IN2P3, Paris, France

¹⁵CEA, Irfu, SPP, Saclay, France

¹⁶IPHC, Université de Strasbourg, CNRS/IN2P3, Strasbourg, France

¹⁷IPNL, Université Lyon 1, CNRS/IN2P3, Villeurbanne, France and Université de Lyon, Lyon, France

¹⁸III. Physikalisches Institut A, RWTH Aachen University, Aachen, Germany

¹⁹Physikalisches Institut, Universität Freiburg, Freiburg, Germany

²⁰II. Physikalisches Institut, Georg-August-Universität Göttingen, Göttingen, Germany

²¹Institut für Physik, Universität Mainz, Mainz, Germany

²²Ludwig-Maximilians-Universität München, München, Germany

²³Panjab University, Chandigarh, India

²⁴Delhi University, Delhi, India

²⁵Tata Institute of Fundamental Research, Mumbai, India

²⁶University College Dublin, Dublin, Ireland

²⁷Korea Detector Laboratory, Korea University, Seoul, Korea

²⁸CINVESTAV, Mexico City, Mexico

²⁹Nikhef, Science Park, Amsterdam, the Netherlands

³⁰Radboud University Nijmegen, Nijmegen, the Netherlands

³¹Joint Institute for Nuclear Research, Dubna, Russia

³²Institute for Theoretical and Experimental Physics, Moscow, Russia

³³Moscow State University, Moscow, Russia

³⁴Institute for High Energy Physics, Protvino, Russia

³⁵Petersburg Nuclear Physics Institute, St. Petersburg, Russia

³⁶Institució Catalana de Recerca i Estudis Avançats (ICREA) and Institut de Física d'Altes Energies (IFAE), Barcelona, Spain

³⁷Uppsala University, Uppsala, Sweden

³⁸Taras Shevchenko National University of Kyiv, Kiev, Ukraine

³⁹Lancaster University, Lancaster LA1 4YB, United Kingdom

⁴⁰Imperial College London, London SW7 2AZ, United Kingdom

⁴¹The University of Manchester, Manchester M13 9PL, United Kingdom

⁴²University of Arizona, Tucson, Arizona 85721, USA

⁴³University of California Riverside, Riverside, California 92521, USA

⁴⁴Florida State University, Tallahassee, Florida 32306, USA

⁴⁵Fermi National Accelerator Laboratory, Batavia, Illinois 60510, USA

⁴⁶University of Illinois at Chicago, Chicago, Illinois 60607, USA

⁴⁷Northern Illinois University, DeKalb, Illinois 60115, USA

⁴⁸Northwestern University, Evanston, Illinois 60208, USA

⁴⁹Indiana University, Bloomington, Indiana 47405, USA

⁵⁰Purdue University Calumet, Hammond, Indiana 46323, USA

⁵¹University of Notre Dame, Notre Dame, Indiana 46556, USA

⁵²Iowa State University, Ames, Iowa 50011, USA

⁵³University of Kansas, Lawrence, Kansas 66045, USA

⁵⁴Louisiana Tech University, Ruston, Louisiana 71272, USA

⁵⁵Northeastern University, Boston, Massachusetts 02115, USA

⁵⁶University of Michigan, Ann Arbor, Michigan 48109, USA

⁵⁷Michigan State University, East Lansing, Michigan 48824, USA

⁵⁸University of Mississippi, University, Mississippi 38677, USA

⁵⁹University of Nebraska, Lincoln, Nebraska 68588, USA

⁶⁰Rutgers University, Piscataway, New Jersey 08855, USA

⁶¹Princeton University, Princeton, New Jersey 08544, USA

⁶²State University of New York, Buffalo, New York 14260, USA

⁶³University of Rochester, Rochester, New York 14627, USA

⁶⁴State University of New York, Stony Brook, New York 11794, USA

⁶⁵Brookhaven National Laboratory, Upton, New York 11973, USA

⁶⁶Langston University, Langston, Oklahoma 73050, USA

⁶⁷University of Oklahoma, Norman, Oklahoma 73019, USA

⁶⁸Oklahoma State University, Stillwater, Oklahoma 74078, USA

⁶⁹Brown University, Providence, Rhode Island 02912, USA

⁷⁰University of Texas, Arlington, Texas 76019, USA

⁷¹Southern Methodist University, Dallas, Texas 75275, USA

⁷²Rice University, Houston, Texas 77005, USA

⁷³University of Virginia, Charlottesville, Virginia 22904, USA

⁷⁴University of Washington, Seattle, Washington 98195, USA

(Dated: 29th October 2014.)

We present a measurement of the distribution of the variable ϕ_η^* for muon pairs with masses between 30 and 500 GeV, using the complete Run II data set collected by the D0 detector at the Fermilab Tevatron proton-antiproton collider. This corresponds to an integrated luminosity of 10.4 fb^{-1} at $\sqrt{s} = 1.96 \text{ TeV}$. The data are corrected for detector effects and presented in bins of dimuon rapidity and mass. The variable ϕ_η^* probes the same physical effects as the Z/γ^* boson transverse momentum, but is less susceptible to the effects of experimental resolution and efficiency. These are the first measurements at any collider of the ϕ_η^* distributions for dilepton masses away from the $Z \rightarrow \ell^+\ell^-$ boson mass peak. The data are compared to QCD predictions based on the resummation of multiple soft gluons.

PACS numbers: 12.38.Qk, 13.85.Qk, 14.70.Hp

Drell-Yan lepton pairs are produced at hadron colliders via quark-antiquark annihilation and may be produced with a non-zero momentum in the plane transverse to the beam direction $p_T^{\ell\ell}$ ($\ell = e, \mu, \tau$) due to QCD radiation from the incoming partons. Measurements of $p_T^{\ell\ell}$ and related variables in events containing Drell-Yan lepton pairs thus allow models of initial state QCD radiation to be tested. Such models are an important component in the phenomenological interpretation of almost all experimental measurements and in searches for new physics at hadron colliders.

In Ref. [1] the D0 Collaboration used the variable ϕ_η^* [2] to study, with unprecedented precision, the $p_T^{\ell\ell}$ distribu-

tion of Z/γ^* bosons in dielectron and dimuon final states with dilepton invariant mass $m_{\ell\ell}$ close to the Z boson pole. The measurements were presented in bins of dilepton rapidity $|y|$ [3]. The variable ϕ_η^* is defined [2] as

$$\phi_\eta^* \equiv \tan(\phi_{\text{acop}}/2) \sin\theta_\eta^*, \quad (1)$$

where ϕ_{acop} is the acoplanarity angle, given by

$$\phi_{\text{acop}} = \pi - \Delta\phi^{\ell\ell}, \quad (2)$$

and $\Delta\phi^{\ell\ell}$ is the difference in azimuthal angle ϕ between the two lepton candidates. Fig. 1 illustrates relevant variables in the plane transverse to the beam direction [1]. The variable θ_η^* is a measure of the scattering angle of the leptons with respect to the proton beam direction in the rest frame of the dilepton system. It is defined [2] by

$$\cos(\theta_\eta^*) = \tanh[(\eta^- - \eta^+)/2], \quad (3)$$

where η^- and η^+ are the pseudorapidities [6] of the negatively and positively charged lepton, respectively. The acoplanarity ϕ_{acop} gives the degree to which the two leptons deviate from being back to back in the plane transverse to the beam direction; it is thus related to $p_T^{\ell\ell}$. Multiplying by $\sin\theta_\eta^*$ in Eq. 1 corrects for the fact that different values of $m_{\ell\ell}$ and $p_T^{\ell\ell}$ will produce different values of ϕ_{acop} depending on the scattering angle of the leptons with respect to the beam direction. The variable

*with visitors from ^aAugustana College, Sioux Falls, SD, USA, ^bThe University of Liverpool, Liverpool, UK, ^cDESY, Hamburg, Germany, ^dUniversidad Michoacana de San Nicolas de Hidalgo, Morelia, Mexico ^eSLAC, Menlo Park, CA, USA, ^fUniversity College London, London, UK, ^gCentro de Investigacion en Computacion - IPN, Mexico City, Mexico, ^hUniversidade Estadual Paulista, São Paulo, Brazil, ⁱKarlsruher Institut für Technologie (KIT) - Steinbuch Centre for Computing (SCC), D-76128 Karlsruhe, Germany, ^jOffice of Science, U.S. Department of Energy, Washington, D.C. 20585, USA, ^kAmerican Association for the Advancement of Science, Washington, D.C. 20005, USA, ^lKiev Institute for Nuclear Research, Kiev, Ukraine, ^mUniversity of Maryland, College Park, Maryland 20742, USA and ⁿEuropean Organization for Nuclear Research (CERN), Geneva, Switzerland

value $a_Z = 1.1 \text{ GeV}^2$). The QCD scales are set event by event to half of the mass of the Z/γ^* boson propagator [10]. The CT10 NNLO parton distribution functions (PDFs) [22] are used and the effects of final state photon radiation (FSR) are taken from PHOTOS [23].

Candidate dimuon events are required to satisfy a trigger based on the identification of a single muon and to contain two reconstructed muons. One of the muons is required to have reconstructed track segments in the muon system tracking detectors both inside and outside the toroidal magnets. The second muon is required to have hits in the muon system or to have an energy deposit in the calorimeter that is consistent with the passage of a minimum-ionizing particle. To ensure an accurate measurement of the muon directions, the two muon candidates are required to be matched to a pair of particle tracks reconstructed in the central tracking detectors with momentum transverse to the beam direction of $p_T > 15 \text{ GeV}$ and $|\eta| < 2$. Candidate muons resulting from misidentified hadrons or produced by the decay of hadrons are suppressed by requiring that they be isolated from other particles observed in either the central tracking detectors or the calorimeters. Requirements are placed on the sum of the p_T of tracks within a cone of $\Delta R = \sqrt{(\Delta\eta)^2 + (\Delta\phi)^2} < 0.5$ around the muon track and on the sum of the E_T of calorimeter clusters within an annulus $0.1 < \Delta R < 0.4$ around the muon track. If more than two muon candidates satisfying the above criteria are found, the two with the highest p_T are considered. The muon tracks are required to be oppositely charged.

Contamination from cosmic ray muons is eliminated by requiring that the muons originate from the $p\bar{p}$ collision point on the basis of their impact parameters and times-of-flight, and by rejecting events in which the two muon candidates are back to back in η within the experimental resolution.

For $70 < m_{\ell\ell} < 110 \text{ GeV}$ a total of 645k dimuon events is selected and the total background fraction, arising mainly from multijet events, is 0.2%.

Away from the Z boson mass peak it is more difficult to obtain samples of well-measured Drell-Yan dimuon events with acceptable levels of background, and additional event selection criteria are imposed. An important source of background in the off-peak samples arises from Drell-Yan dimuon events that originate close to the Z boson mass peak, but are reconstructed with a value of $m_{\ell\ell}$ away from the Z boson mass peak due to FSR or to the mis-measurement of the p_T of one of the muon candidates. We refer below to such events as ‘‘migration background’’. The level of migration background in the off-peak signal samples is estimated using MC and is cross checked using control samples in the data.

Below the Z boson mass peak, dimuon events are selected with $30 < m_{\ell\ell} < 60 \text{ GeV}$. To increase the event selection efficiency in this low mass region and to reduce

any kinematic bias on the distribution of ϕ_η^* , the selection criteria are relaxed: we require the leading muon to satisfy $p_T > 15 \text{ GeV}$, but allow the second muon to satisfy $p_T > 10 \text{ GeV}$. The dominant backgrounds in the $30 < m_{\ell\ell} < 60 \text{ GeV}$ sample arise from $Z/\gamma^* \rightarrow \tau^-\tau^+$ and migration. Background from $Z/\gamma^* \rightarrow \tau^-\tau^+$ events containing hadronically decaying τ leptons is suppressed by applying isolation criteria on the muon candidates that are more stringent than those used for the $70 < m_{\ell\ell} < 110 \text{ GeV}$ event sample. In particular, an additional requirement is placed on the sum of the E_T of calorimeter clusters within a cone $\Delta R < 0.1$ around the muon track. The fraction of the selected event sample arising from $Z/\gamma^* \rightarrow \tau^-\tau^+$ background is estimated to be 5.2%. Migration background from events that originate close to the Z boson mass peak but are reconstructed with $30 < m_{\ell\ell} < 60 \text{ GeV}$ due to FSR is suppressed by excluding events that contain an isolated photon candidate with $p_T > 15 \text{ GeV}$. Migration background from the Z boson mass peak can also arise from events in which the p_T of one of the muon candidates is underestimated. This background is suppressed using a ‘‘pseudo-mass’’ variable, m_{pseudo} : the invariant mass of the muon pair is recalculated having set the magnitude of the p_T of the lower p_T muon to be equal to that of the higher p_T muon. This is under the hypothesis that if an event originates close to the Z boson mass peak, but is reconstructed with $30 < m_{\ell\ell} < 60 \text{ GeV}$, the p_T of the lower p_T muon candidate has been underestimated. Migration background events tend to have large values of m_{pseudo} and candidate events are required to satisfy $m_{\text{pseudo}} < 75 \text{ GeV}$. This requirement rejects only 2% of Drell-Yan dimuon events with $30 < m_{\ell\ell} < 60 \text{ GeV}$ at the generator level. The fraction of the selected event sample arising from migration background from Drell-Yan dimuon events for which the generator-level Z/γ^* boson propagator mass is greater than 70 GeV is estimated to be 1.3%. Remaining backgrounds amount to 1.6% of the selected event sample and arise mainly from multijet events. A total of 74k dimuon events is selected for $30 < m_{\ell\ell} < 60 \text{ GeV}$.

Above the Z boson mass peak, dimuon events are selected within the two mass ranges $160 < m_{\ell\ell} < 300 \text{ GeV}$ and $300 < m_{\ell\ell} < 500 \text{ GeV}$. In these samples the only significant source of contamination arises from the moderate resolution in p_T (and thus $m_{\ell\ell}$) in the compact central tracking detectors of DØ. The level of bin migration in $m_{\ell\ell}$ in Drell-Yan dimuon events is reduced by imposing tight requirements on the number of silicon microstrip and central fiber tracker hits associated with the muon tracks and the χ^2 of the track fits. Bin migration in $m_{\ell\ell}$ is further suppressed by rejecting events in which there is a very large asymmetry between the magnitudes of the p_T of the two muons. For the mass ranges $160 < m_{\ell\ell} < 300 \text{ GeV}$ and $300 < m_{\ell\ell} < 500 \text{ GeV}$, respectively, the numbers of selected events are 1744 and 207, and the fractions of the selected event samples aris-

ing from bin migration in $m_{\ell\ell}$ are estimated to be 24% and 44%.

The observed ϕ_η^* distributions are corrected for background, and for experimental efficiency and resolution. Backgrounds from $Z/\gamma^* \rightarrow \tau^-\tau^+$, $W \rightarrow \ell\nu$ (+jets), $WW \rightarrow \ell\nu\ell\nu$, top quark pairs and multijet events are subtracted from the observed ϕ_η^* distributions. The corrections to the background-subtracted ϕ_η^* distribution for experimental efficiency and resolution (including the effect of bin migration in $m_{\ell\ell}$) are evaluated using fully simulated dimuon MC events. When evaluating the correction factors, we apply at the MC particle level the same kinematic selection criteria on $m_{\ell\ell}$, muon p_T , and $|\eta|$ as in the selection of the data, as specified above. For this purpose, MC particle-level muons are defined after QED final state radiation, which mimics the measurement of muon momentum in the tracking detector. In addition, in the low mass dimuon sample ($30 < m_{\ell\ell} < 60$ GeV) events are rejected if they contain an FSR photon with transverse energy $E_T^\gamma > 14$ GeV; this is in order to mimic the selection criteria on isolated photons and muon isolation applied at the detector level.

Since the experimental resolution in ϕ_η^* is narrower than the chosen bin widths, the fractions of accepted events that fall within the same bin in ϕ_η^* at the particle level and reconstructed detector level in the MC are high, having typical (lowest) values of around 98% (92%). Therefore, simple bin-by-bin corrections of the ϕ_η^* distribution are sufficient.

The fully simulated Drell-Yan dimuon MC events used to calculate the detector corrections are re-weighted at the generator level in two dimensions ($p_T^{\ell\ell}$ and $|y|$) to match the predictions of RESBOS. In addition, adjustments are made to improve the accuracy of the following aspects of the detector simulation: muon p_T scale and resolution, track ϕ and η resolutions, trigger efficiencies, and relevant offline reconstruction and selection efficiencies. Variations in the above adjustments to the underlying physics and the detector simulation are included in the assessment of the systematic uncertainties on the correction factors. Because of the high bin purities, the systematic uncertainties on the correction factors arising from variations in the assumed underlying ϕ_η^* distribution are found to be negligible.

The systematic uncertainties due to muon p_T scale and resolution are small, and arise only due to the kinematic requirements in the event selection. The measured ϕ_η^* distribution is, however, susceptible to modulations in ϕ of the muon identification and trigger efficiencies, which result, e.g., from detector module boundaries in the muon system. Particular care has been taken in the choice of muon identification criteria in order to minimize such modulations and also to ensure that such modulations are well simulated in the MC. For example, the inclusion of muon candidates identified in the calorimeter reduces the effect of gaps between modules in the outer muon

system. Nevertheless, accurate modeling of the residual inefficiencies in the inter-module regions is verified, since this is particularly important in this measurement; regions of low efficiency that are back-to-back in ϕ cause the efficiency to modulate as a function of ϕ_η^* . Accurate modeling of the angular resolution of the central tracking detectors is another crucial aspect of this analysis. The resolution in ϕ and η is measured in the data using cosmic ray muons that traverse the detector, since these should produce events containing two tracks that are exactly back to back except for the effect of detector resolution.

Control samples in which one or more of the event selection criteria are relaxed or inverted are used to test the predicted levels of background in the off-peak dimuon samples and to assess the associated systematic uncertainties. The level of background in the $30 < m_{\ell\ell} < 60$ GeV sample arising from $Z/\gamma^* \rightarrow \tau^-\tau^+$ events containing hadronically decaying τ leptons is verified by checking that the simulation provides a good description of the sum of the E_T of calorimeter clusters within $\Delta R < 0.1$ around the muon track. In addition, hadrons misidentified as muons are less likely than genuine muons to be associated with reconstructed track segments in the muon system both inside and outside the toroidal magnets. The number and kinematic properties of events containing only one such muon candidate, which are enriched in $Z/\gamma^* \rightarrow \tau^-\tau^+$ events containing hadronically decaying τ leptons, are found to be reasonably well described.

The predicted levels of migration background in the off-peak samples are cross checked using control samples. For $30 < m_{\ell\ell} < 60$ GeV the number and kinematic properties of the events exclusively rejected by the veto on isolated photons are well described. The selection criteria on m_{pseudo} (for $30 < m_{\ell\ell} < 60$ GeV) and the asymmetry between the magnitudes of the p_T of the two muons (for $160 < m_{\ell\ell} < 300$ GeV and $300 < m_{\ell\ell} < 500$ GeV) introduce a bias on the ϕ_η^* distributions of the selected event samples, which has to be accounted for in the MC-derived correction factors. It has been verified that the distributions in m_{pseudo} and the p_T asymmetry, having applied all other selection cuts, are reasonably well described by the MC.

Systematic uncertainties on the corrections applied to the data arise from residual uncertainties in the modeling of the detector response and the levels of backgrounds. The following are varied within their uncertainties: muon p_T scale and resolution; dependence of trigger and offline identification efficiencies on η and on the proximity to detector module boundaries in ϕ . Systematic uncertainties on the levels of backgrounds are assigned to cover the statistical uncertainties of the cross checks using control samples, as well as any residual data-MC discrepancies revealed by these cross checks. The total experimental systematic uncertainty is evaluated as the quadrature

sum of all the uncertainties discussed above. In almost all ϕ_η^* bins the total experimental systematic uncertainty is substantially smaller than the statistical uncertainty.

The QCD scale uncertainties for the RESBOS predictions are evaluated by varying the renormalization scale or the factorization scale by a factor of two [10]. For the NNLL+NLO predictions, the theoretical uncertainties are assessed by variations in renormalization scale, factorization scale and resummation scale between $m_{\ell\ell}/2$ and $2m_{\ell\ell}$, with the additional requirement that the ratio of any two of these scales lies between 1/2 and 2 [8].

Figure 2 shows the normalized dimuon ϕ_η^* distributions $(1/\sigma) \times (d\sigma/d\phi_\eta^*)$ in two bins of dimuon $|y|$ corrected to the particle level for the kinematic region: $70 < m_{\ell\ell} < 110$ GeV, and for both muons $p_T > 15$ GeV and $|\eta| < 2$. The data are compared to predictions from RESBOS for the same particle-level kinematic region and in the same bins used for the experimental data. The values of $(1/\sigma) \times (d\sigma/d\phi_\eta^*)$ are plotted at the center of the relevant bin in ϕ_η^* .

Figure 3 shows the ratio of the corrected ϕ_η^* distributions to the RESBOS predictions for $70 < m_{\ell\ell} < 110$ GeV. In addition to the dimuon data from the present analysis, the dielectron data from Ref. [1] are shown [24]. Given that the experimental corrections are very different in the two channels, the consistency of the dielectron and dimuon measurements represents a powerful cross check of the corrected distributions.

Figure 4 shows for $70 < m_{\ell\ell} < 110$ GeV the ratio of the corrected dimuon data to the NNLL+NLO predictions of Ref. [8]. In addition to the dimuon data from the present analysis, the dielectron data from Ref. [1] are shown. The NLO PDF sets CTEQ6m [25] are implemented in this calculation. The NNLL+NLO predictions of Ref. [8] do not include the effects of FSR. The lack of FSR has a greater effect on the predictions for dielectrons than for dimuons and leads to a poorer level of agreement between the dielectron and dimuon data than was observed in Figure 3.

Figures 3 and 4 show that the theoretical uncertainties arising from QCD scale variations and PDFs are large compared to the experimental uncertainties. Within the quoted uncertainties both predictions are consistent with the corrected data. Figure 5 shows the ratio of the $(1/\sigma)(d\sigma/d\phi_\eta^*)$ distribution in the central rapidity region ($|y| < 1$) to that in the forward rapidity region ($1 < |y| < 2$). The corrected dimuon data are compared to the predictions from RESBOS [10] and from the NNLL+NLO calculations [8]. Figure 5 shows that the theoretical uncertainties largely cancel in this ratio and that the predictions are consistent with the data.

Figure 6 shows the normalized dimuon ϕ_η^* distributions $(1/\sigma) \times (d\sigma/d\phi_\eta^*)$ in two bins of $|y|$, corrected to the particle level with kinematic requirements: $30 < m_{\ell\ell} < 60$ GeV, and for both muons $p_T > 10$ GeV and $|\eta| < 2$, with one muon required to satisfy $p_T > 15$ GeV. In ad-

dition, events are required at particle level to contain no FSR photon with transverse energy $E_T^\gamma > 14$ GeV. The data are compared to predictions from RESBOS [10] with the same particle-level kinematic cuts applied.

Figure 7 shows the ratio of the corrected ϕ_η^* distributions to the RESBOS predictions for $30 < m_{\ell\ell} < 60$ GeV. Figure 8 shows the ratio of the same data to the NNLL+NLO predictions of Ref. [8, 26]. At high values of ϕ_η^* the prediction from RESBOS agrees less well with data than is the case in the region of the Z boson mass peak. A known deficiency of the RESBOS prediction for $\phi_\eta^* > 0.5$ in the low mass region is the absence of the NNLO correction factor for the photon exchange diagram.

Figure 9 shows the normalized dimuon ϕ_η^* distributions $(1/\sigma) \times (d\sigma/d\phi_\eta^*)$, corrected to the particle level with kinematic requirements: $160 < m_{\ell\ell} < 300$ GeV and $300 < m_{\ell\ell} < 500$ GeV, and for both muons $p_T > 15$ GeV and $|\eta| < 2$. The data are compared to predictions from RESBOS with the same particle-level kinematic requirements applied. Figure 10 shows the ratios of the corrected ϕ_η^* distributions to the RESBOS predictions. Within the fairly large statistical uncertainties, the predictions are consistent with the corrected data.

The corrected distributions of $(1/\sigma) \times (d\sigma/d\phi_\eta^*)$ in the two dimuon mass ranges $30 < m_{\ell\ell} < 60$ GeV and $70 < m_{\ell\ell} < 130$ GeV are compared in Fig. 11. As discussed above, the width of the ϕ_η^* distribution is expected to decrease with increasing $m_{\ell\ell}$. Fig. 11 shows that the data are consistent with this expectation and that RESBOS provides a good description of this behavior. The numbers of selected events in the dimuon mass ranges $160 < m_{\ell\ell} < 300$ GeV and $300 < m_{\ell\ell} < 500$ GeV are insufficient to allow us to present the distributions of $(1/\sigma) \times (d\sigma/d\phi_\eta^*)$ in the two separate ranges of $|y|$ shown in Fig. 11. However, the dependence on $|y|$ is small and a comparison between Figs. 9 and 11 shows that the distributions of $(1/\sigma) \times (d\sigma/d\phi_\eta^*)$ continue to become more narrow with increasing dimuon mass in the region above the Z boson mass peak.

In summary, using 10.4 fb^{-1} of $p\bar{p}$ collisions we have measured the normalized ϕ_η^* distribution $(1/\sigma) \times (d\sigma/d\phi_\eta^*)$ in two bins of dimuon rapidity and four bins of dimuon mass. Relative to the results presented in Ref. [1], these measurements in the dimuon channel represent an extension to the full D0 data set and also to regions of dimuon mass away from the Z boson mass peak. The data are well described within the theoretical uncertainties by the RESBOS MC and by the predictions at NNLL+NLO accuracy of Ref. [8, 26]. In the Z boson mass peak region, $70 < m_{\ell\ell} < 110$ GeV, the theoretical uncertainties shown in Figs. 3 and 4 are large compared to the experimental uncertainties. Figure 5 shows the ratio of the $(1/\sigma)(d\sigma/d\phi_\eta^*)$ distribution in the central rapidity region ($|y| < 1$) to that in the forward rapidity region ($1 < |y| < 2$). The theoretical uncertain-

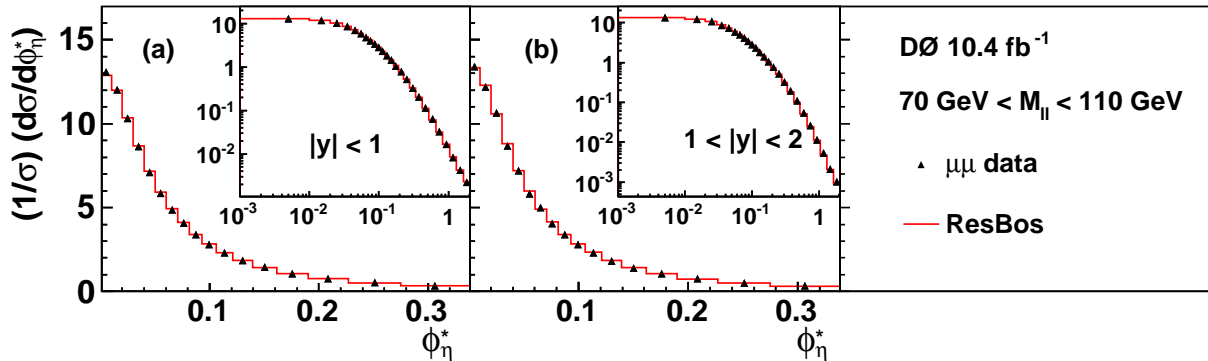


FIG. 2: (color online) Corrected distributions of $(1/\sigma) \times (d\sigma/d\phi_\eta^*)$ in dimuon events with $70 < m_{\ell\ell} < 110$ GeV for (a) $|y| < 1$ and (b) $1 < |y| < 2$ in the restricted range $0 < \phi_\eta^* < 0.34$. The insets show an extended range of ϕ_η^* . The error bars on the data points represent statistical and systematic uncertainties combined in quadrature. The predictions from RESBOS [10] are shown as histograms.

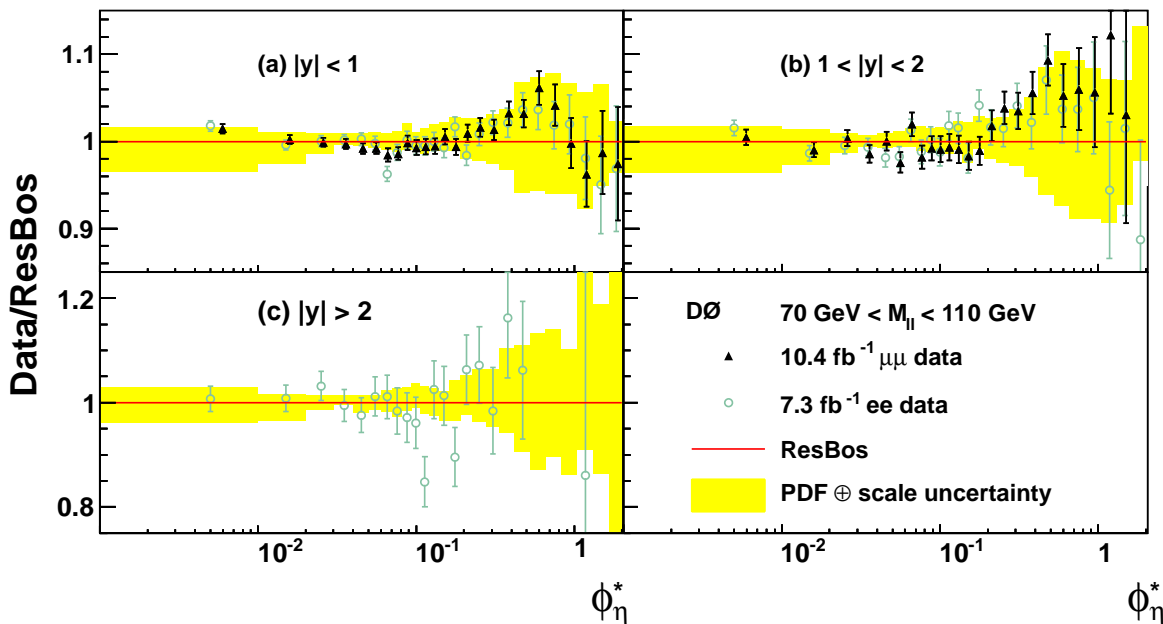


FIG. 3: (color online) Ratio of the corrected distributions of $(1/\sigma) \times (d\sigma/d\phi_\eta^*)$ in dielectron and dimuon data to the predictions of RESBOS [10] for $70 < m_{\ell\ell} < 110$ GeV for (a) $|y| < 1$, (b) $1 < |y| < 2$, and (c) $|y| > 2$. The error bars on the data points represent statistical and systematic uncertainties combined in quadrature. The dielectron data are taken from Ref. [1] and correspond to an integrated luminosity of 7.3 fb^{-1} . The band around the RESBOS prediction represents the quadrature sum of uncertainties due to PDFs (evaluated using the CT10 NNLO error PDF sets [22]) and the QCD scale (evaluated by varying the factorization and renormalization scales).

ties largely cancel in this ratio and the QCD predictions are consistent with the data. The data are consistent with the expectation that the width of the ϕ_η^* distribution decreases with increasing $m_{\ell\ell}$. The measurements of ϕ_η^* distributions above the Z boson mass peak may help constrain systematic uncertainties arising from initial state gluon bremsstrahlung in analyses of other high mass final states, such as those containing top quarks.

Tables of corrected $(1/\sigma) \times (d\sigma/d\phi_\eta^*)$ distributions for

each $|y|$ bin and range of $m_{\ell\ell}$ are provided in the appendix. In some of these tables results are given for a larger range of ϕ_η^* than is shown in the corresponding figures.

We thank the authors of Refs. [10] and [8], in particular Marco Guzzi and Lee Tomlinson, respectively, for their help in evaluating predictions to be compared with the new off-peak measurements. We thank the staffs at Fermilab and collaborating institutions, and acknowl-

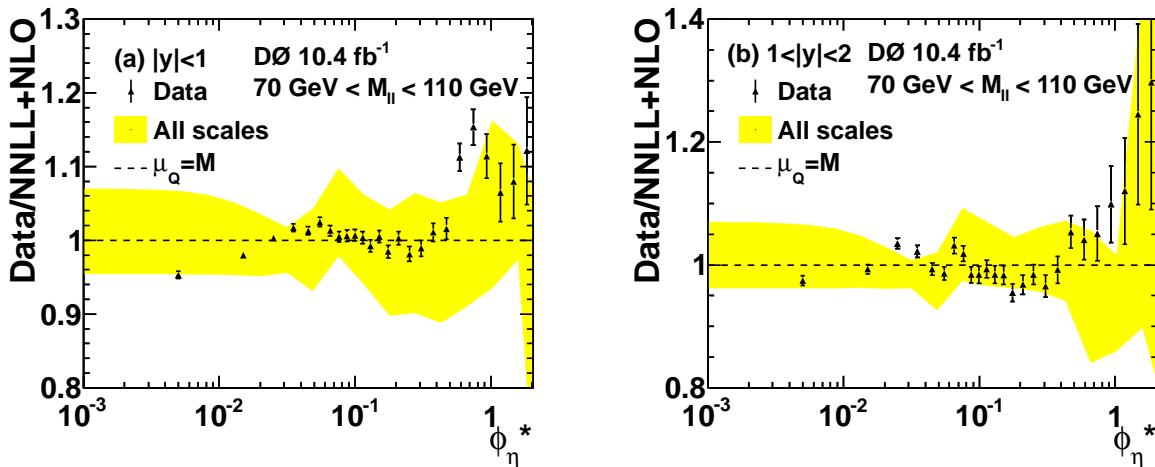


FIG. 4: (color online) Ratio of the corrected distributions of $(1/\sigma) \times (d\sigma/d\phi_\eta^*)$ in dielectron and dimuon data to the NNLL+NLO predictions of Ref. [8] for $70 < m_{\ell\ell} < 110$ GeV: (a) $|y| < 1$ and (b) $1 < |y| < 2$. The error bars on the data points represent statistical and systematic uncertainties combined in quadrature. The dielectron data are taken from Ref. [1] and correspond to an integrated luminosity of 7.3 fb^{-1} . The band around the NNLL+NLO prediction represents the uncertainty due to variations in the QCD scales (evaluated by varying the resummation, factorization and renormalization scales).

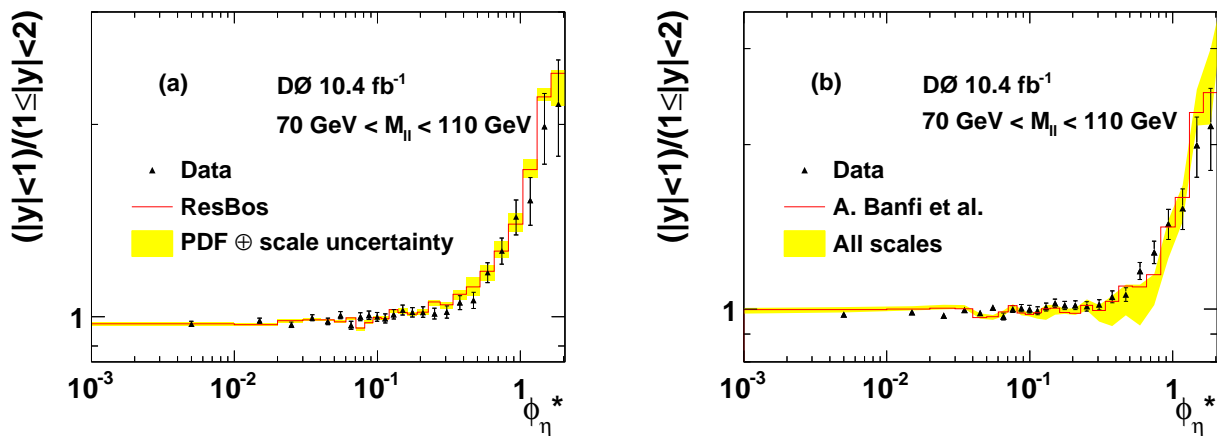


FIG. 5: (color online) Ratio of the $(1/\sigma)(d\sigma/d\phi_\eta^*)$ distribution in the central rapidity region ($|y| < 1$) to that in the forward rapidity region ($1 < |y| < 2$). The corrected dimuon data are compared to the predictions from (a) RESBOS [10] and from (b) NNLL+NLO [8]. The error bars on the data points represent statistical and systematic uncertainties combined in quadrature, assuming no correlation between the two rapidity regions. The theoretical predictions are represented by histograms and the band shows the theoretical uncertainties, taking correlations between the two rapidity regions into account.

edge support from the Department of Energy and National Science Foundation (United States of America); Alternative Energies and Atomic Energy Commission and National Center for Scientific Research/National Institute of Nuclear and Particle Physics (France); Ministry of Education and Science of the Russian Federation, National Research Center “Kurchatov Institute”

of the Russian Federation, and Russian Foundation for Basic Research (Russia); National Council for the Development of Science and Technology and Carlos Chagas Filho Foundation for the Support of Research in the State of Rio de Janeiro (Brazil); Department of Atomic Energy and Department of Science and Technology (India); Administrative Department of Science,

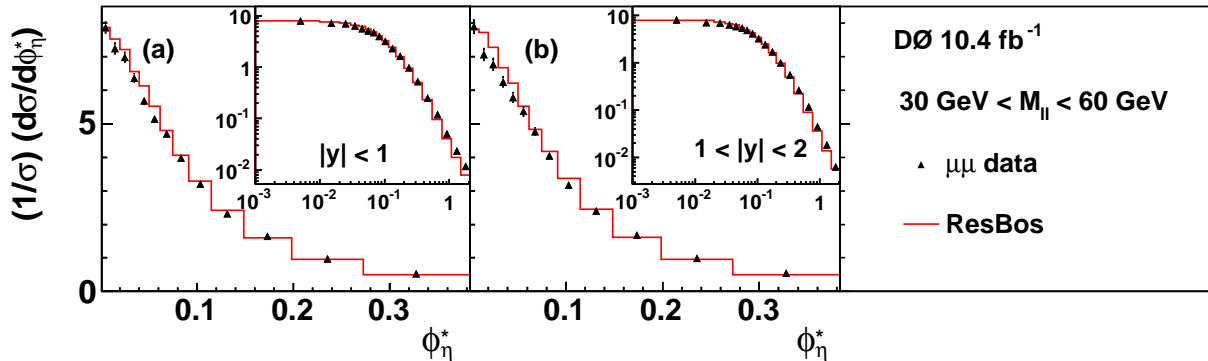


FIG. 6: (color online) Corrected distributions of $(1/\sigma) \times (d\sigma/d\phi_\eta^*)$ in dimuon events with $30 < m_{\ell\ell} < 60$ GeV for (a) $|y| < 1$ and (b) $1 < |y| < 2$ in the restricted range $0 < \phi_\eta^* < 0.38$. The insets show an extended range of ϕ_η^* . The error bars on the data points represent statistical and systematic uncertainties combined in quadrature. The predictions from RESBOS [10] are shown as histograms.

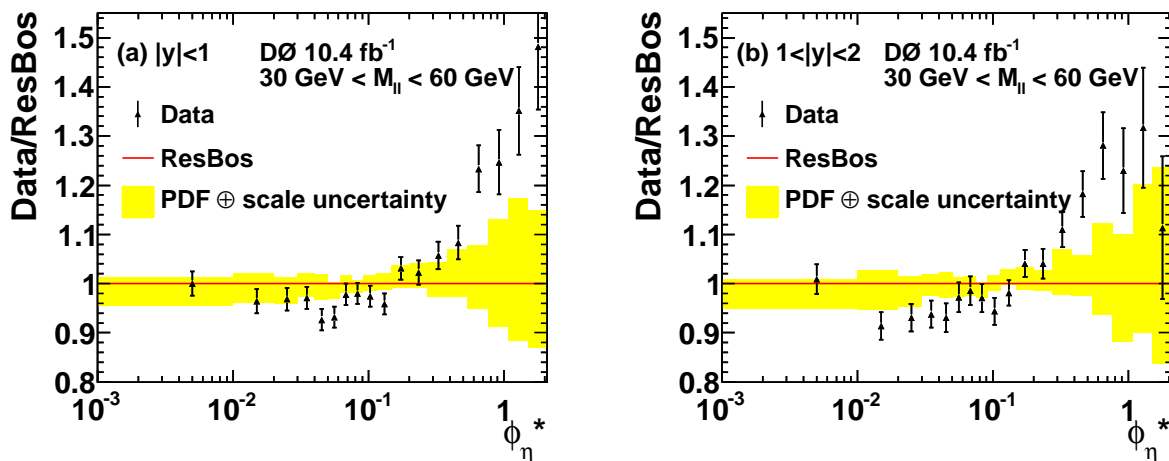


FIG. 7: (color online) Ratio of the corrected distributions of $(1/\sigma) \times (d\sigma/d\phi_\eta^*)$ to RESBOS [10] in dimuon events with $30 < m_{\ell\ell} < 60$ GeV for (a) $|y| < 1$ and (b) $1 < |y| < 2$. Statistical and systematic uncertainties are combined in quadrature. The band around the RESBOS prediction represents the quadrature sum of uncertainties due to PDFs (evaluated using the CT10 NNLO error PDF sets [22]) and the QCD scale (evaluated by varying the factorization and renormalization scales).

Technology and Innovation (Colombia); National Council of Science and Technology (Mexico); National Research Foundation of Korea (Korea); Foundation for Fundamental Research on Matter (The Netherlands); Science and Technology Facilities Council and The Royal Society (United Kingdom); Ministry of Education, Youth and Sports (Czech Republic); Bundesministerium für Bildung und Forschung (Federal Ministry of Education and Research) and Deutsche Forschungsgemeinschaft (German Research Foundation) (Germany); Science Foundation Ireland (Ireland); Swedish Research Council (Sweden); China Academy of Sciences and National Natural Science Foundation of China (China); and Ministry of Education and Science of Ukraine (Ukraine).

- [1] D0 Collaboration, V. M. Abazov *et al.*, Phys. Rev. Lett. **106**, 122001 (2011).
- [2] A. Banfi, S. Redford, M. Vesterinen, P. Waller, and T. R. Wyatt, Eur. Phys. J. C **71**, 1600 (2011).
- [3] The dilepton rapidity is defined by $y = (1/2) \ln [(E + p_z)/(E - p_z)]$, where E is the energy and p_z is the momentum component parallel to the proton beam direction. The rapidity is given in terms of the momentum fractions, x_1 and x_2 of the annihilating quark and antiquark by $y = (1/2) \ln (x_1/x_2)$.
- [4] M. Vesterinen and T. R. Wyatt, Nucl. Instr. and Meth. Phys. Res. A **602**, 432 (2009).
- [5] The thrust axis is defined as a unit vector in the direction of $\vec{p}_T^{(\text{lepton1})} - \vec{p}_T^{(\text{lepton2})}$, where $\vec{p}_T^{(\text{lepton1})}$ and $\vec{p}_T^{(\text{lepton2})}$ are

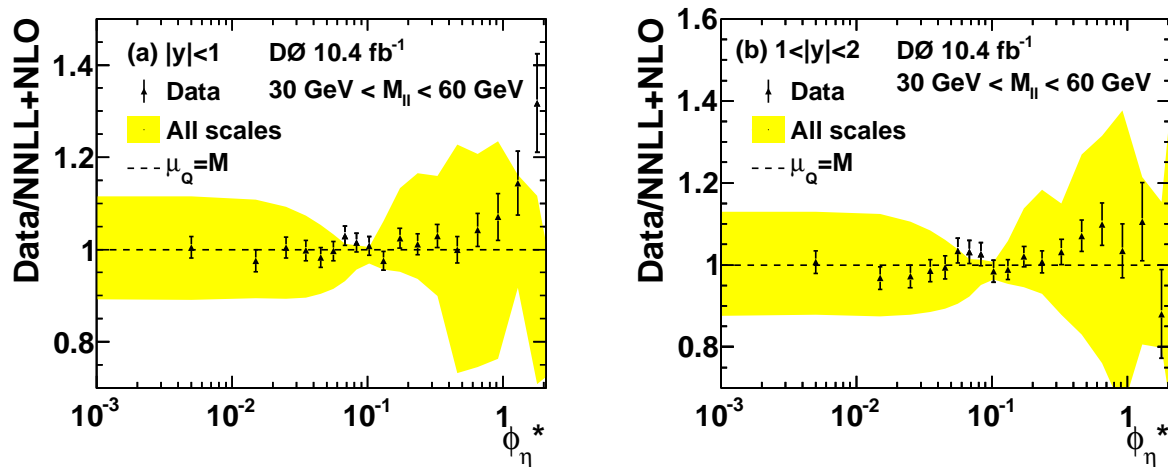


FIG. 8: (color online) Ratio of the corrected distributions of $(1/\sigma) \times (d\sigma/d\phi_\eta^*)$ to the NNLL+NLO predictions of Ref. [8, 26] in dimuon events with $30 < m_{\ell\ell} < 60$ GeV for (a) $|y| < 1$ and (b) $1 < |y| < 2$. Statistical and systematic uncertainties are combined in quadrature. The band around the NNLL+NLO prediction represents the uncertainty due to variations in the QCD scales (evaluated by varying the resummation, factorization and renormalization scales).

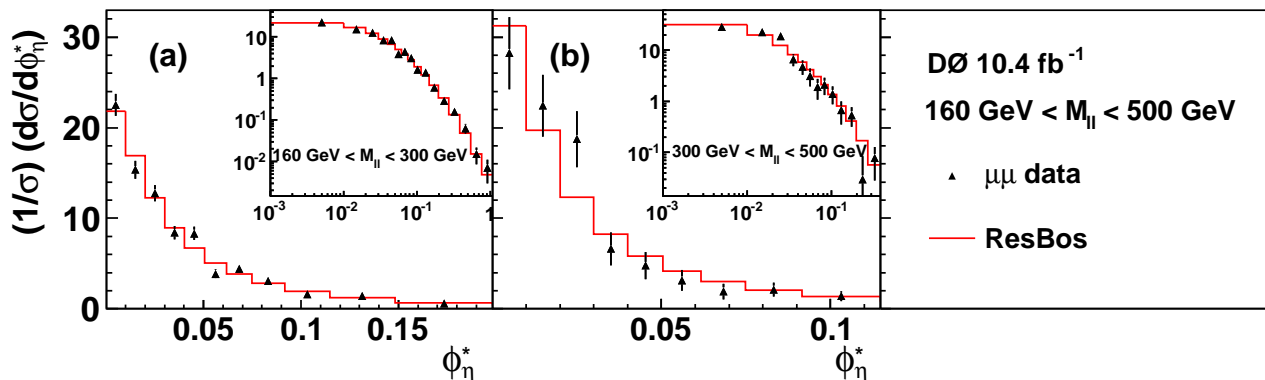


FIG. 9: (color online) Corrected distributions of $(1/\sigma) \times (d\sigma/d\phi_\eta^*)$ for dimuon events with (a) $160 < m_{\ell\ell} < 300$ GeV and (b) $300 < m_{\ell\ell} < 500$ GeV for a restricted range of ϕ_η^* . The insets show an extended range of ϕ_η^* . The error bars on the data points represent statistical and systematic uncertainties combined in quadrature. The predictions from RESBOS [10] are shown as the red histogram.

- the lepton momentum vectors in the transverse plane.
- [6] Pseudorapidity is defined by $\eta = -\ln[\tan(\theta/2)]$, where θ is the polar angle with respect to the proton beam direction.
- [7] A. Banfi, M. Dasgupta, and S. Marzani, Phys. Lett. B **701**, 75 (2011).
- [8] A. Banfi, M. Dasgupta, S. Marzani, and L. Tomlinson, J. High Energy Phys. **01**, 044 (2011).
- [9] J. M. Campbell and R. K. Ellis, Phys. Rev. D **65**, 113007 (2002).
- [10] M. Guzzi, P. M. Nadolsky, and B. Wang, Phys. Rev. D **90**, 014030 (2014).
- [11] A. Banfi, M. Dasgupta, S. Marzani, and L. Tomlinson, Phys. Lett. B **715**, 152 (2012).
- [12] ATLAS Collaboration, G. Aad *et al.*, Phys. Lett. B **720**, 32 (2013).
- [13] LHCb Collaboration, R. Aaij *et al.*, J. High Energy Phys. **02**, 106 (2013).
- [14] J. Collins, D. Soper, and G. Sterman, Nucl. Phys. B **250**, 199 (1985).
- [15] D0 Collaboration, V. M. Abazov *et al.*, Nucl. Instrum. Methods Phys. Res. A **565**, 463 (2006); M. Abolins *et al.*, Nucl. Instrum. Methods Phys. Res. A **584**, 75 (2008); R. Angstadt *et al.*, Nucl. Instrum. Methods Phys. Res. A **622**, 298 (2010).
- [16] D0 Collaboration, S. Abachi *et al.*, Nucl. Instrum. Methods Phys. Res. A **338**, 185 (1994).
- [17] V. M. Abazov *et al.*, Nucl. Instrum. Methods Phys. Res. A **552**, 372 (2005).
- [18] T. Sjöstrand *et al.*, Comp. Phys. Comm. **135**, 238 (2001).
- [19] R. Brun and F. Carminati, CERN Program Library Long Writeup W5013, 1993 (unpublished).

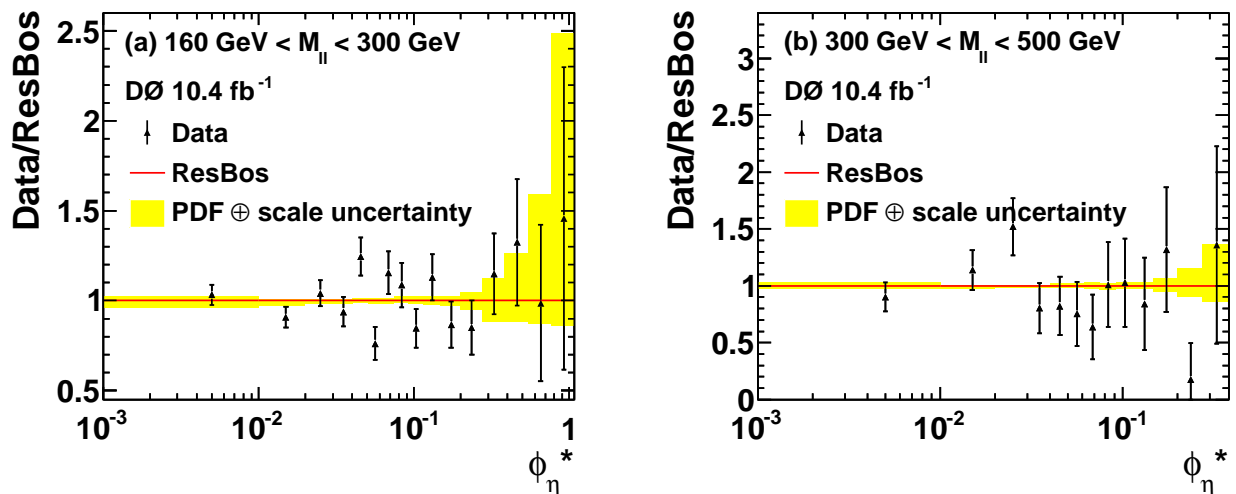


FIG. 10: (color online) Ratio of the corrected distributions of $(1/\sigma) \times (d\sigma/d\phi_\eta^*)$ to RESBOS [10] for (a) $160 < m_{\ell\ell} < 300$ GeV and (b) $300 < m_{\ell\ell} < 500$ GeV. Statistical and systematic uncertainties are combined in quadrature. The band around the RESBOS prediction represents the quadrature sum of uncertainties due to PDFs (evaluated using the CT10 NLO error PDF sets [22]) and the QCD scale (evaluated by varying the factorization and renormalization scales).

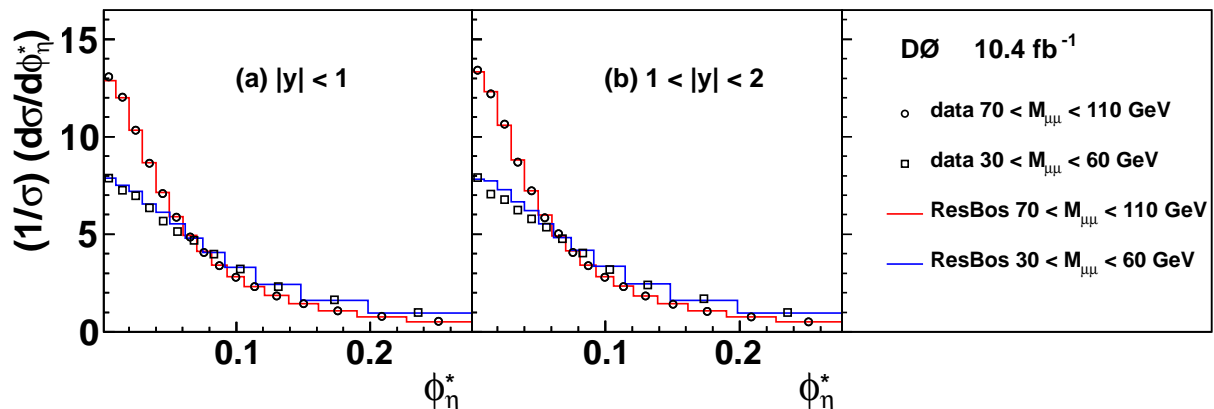


FIG. 11: (color online) Comparison of corrected distributions of $(1/\sigma) \times (d\sigma/d\phi_\eta^*)$ in dimuon events with $30 < m_{\ell\ell} < 60$ GeV and $70 < m_{\ell\ell} < 130$ GeV for (a) $|y| < 1$ and (b) $1 < |y| < 2$ in the restricted range $0 < \phi_\eta^* < 0.28$. The error bars on the data points represent statistical and systematic uncertainties combined in quadrature. The predictions from RESBOS [10] are shown as histograms.

- [20] M. L. Mangano *et al.*, J. High Energy Phys. **07**, 001 (2003).
- [21] C. Balazs and C.-P. Yuan, Phys. Rev. D **56**, 5558 (1997).
- [22] J. Gao, M. Guzzi, J. Huston, H.-L. Lai, Z. Li, P. M. Nadolsky, J. Pumplin, D. Stump and C.-P. Yuan, arXiv: 1302.6246 (2013).
- [23] E. Barberio and Z. W̄as, Comput. Phys. Commun. **79**, 291 (1994).
- [24] Following Ref. [1] the momentum of MC particle-level electrons are defined as the full-momentum vector sum of any photons or electrons within a cone of $\Delta R = \sqrt{(\Delta\eta)^2 + (\Delta\phi)^2} < 0.2$ around the electron, where $\Delta\eta$ ($\Delta\phi$) is the distance in η (ϕ) from the particle-level electron. The dielectron kinematic requirements are: $70 <$

$m_{\ell\ell} < 110$ GeV, and for both electrons $p_T > 20$ GeV and $|\eta| < 1.1$ or $1.5 < |\eta| < 3$.

- [25] J. Pumplin, D. R. Stump, J. Huston, H. L. Lai, P. Nadolsky, and W. K. Tung, hep-ph/0201195.
- [26] L. Tomlinson, private communications.

Appendix: Tables of results

TABLE I: Table of results for the dimuon channel for $|y| < 1$ region with $70 < m_{\ell\ell} < 110$ GeV. The first quoted uncertainty is statistical and the second is the total experimental systematic uncertainty.

bin	ϕ_η^* range	$1/\sigma \, d\sigma/d\phi_\eta^*$
1	0.000–0.010	$13.069 \pm 0.052 \pm 0.039$
2	0.010–0.020	$12.017 \pm 0.049 \pm 0.027$
3	0.020–0.030	$10.334 \pm 0.046 \pm 0.012$
4	0.030–0.040	$8.652 \pm 0.042 \pm 0.016$
5	0.040–0.050	$7.100 \pm 0.038 \pm 0.008$
6	0.050–0.060	$5.869 \pm 0.034 \pm 0.013$
7	0.060–0.071	$4.863 \pm 0.031 \pm 0.016$
8	0.071–0.081	$4.068 \pm 0.028 \pm 0.007$
9	0.081–0.093	$3.399 \pm 0.024 \pm 0.009$
10	0.093–0.106	$2.803 \pm 0.021 \pm 0.006$
11	0.106–0.121	$2.303 \pm 0.018 \pm 0.006$
12	0.121–0.139	$1.843 \pm 0.014 \pm 0.005$
13	0.139–0.162	$1.442 \pm 0.011 \pm 0.004$
14	0.162–0.190	$1.067 \pm 0.009 \pm 0.003$
15	0.190–0.227	$0.778 \pm 0.007 \pm 0.002$
16	0.227–0.275	$0.524 \pm 0.005 \pm 0.002$
17	0.275–0.337	$0.332 \pm 0.003 \pm 0.002$
18	0.337–0.418	$0.204 \pm 0.002 \pm 0.001$
19	0.418–0.523	$0.115 \pm 0.002 \pm 0.001$
bin	range	$1/\sigma \times (d\sigma/d\phi_\eta^*)(\times 100)$
20	0.523–0.657	$6.428 \pm 0.099 \pm 0.040$
21	0.657–0.827	$3.310 \pm 0.064 \pm 0.029$
22	0.827–1.041	$1.673 \pm 0.041 \pm 0.019$
23	1.041–1.309	$0.818 \pm 0.026 \pm 0.016$
24	1.309–1.640	$0.420 \pm 0.017 \pm 0.010$
25	1.640–2.049	$0.225 \pm 0.011 \pm 0.010$
26	2.049–2.547	$0.120 \pm 0.007 \pm 0.005$
27	2.547–3.151	$0.076 \pm 0.005 \pm 0.004$
28	3.151–3.878	$0.044 \pm 0.004 \pm 0.003$
29	3.878–4.749	$0.026 \pm 0.003 \pm 0.001$

TABLE II: Table of results for the dimuon channel for $1 < |y| < 2$ region with $70 < m_{\ell\ell} < 110$ GeV. The first quoted uncertainty is statistical and the second is the total experimental systematic uncertainty.

bin	ϕ_η^* range	$1/\sigma d\sigma/d\phi_\eta^*$
1	0.000–0.010	$13.404 \pm 0.094 \pm 0.056$
2	0.010–0.020	$12.189 \pm 0.090 \pm 0.036$
3	0.020–0.030	$10.635 \pm 0.084 \pm 0.027$
4	0.030–0.040	$8.685 \pm 0.076 \pm 0.030$
5	0.040–0.050	$7.218 \pm 0.069 \pm 0.022$
6	0.050–0.060	$5.836 \pm 0.062 \pm 0.017$
7	0.060–0.071	$5.013 \pm 0.057 \pm 0.027$
8	0.071–0.081	$4.065 \pm 0.050 \pm 0.011$
9	0.081–0.093	$3.382 \pm 0.044 \pm 0.009$
10	0.093–0.106	$2.802 \pm 0.038 \pm 0.010$
11	0.106–0.121	$2.317 \pm 0.032 \pm 0.007$
12	0.121–0.139	$1.827 \pm 0.026 \pm 0.007$
13	0.139–0.162	$1.407 \pm 0.020 \pm 0.008$
14	0.162–0.190	$1.050 \pm 0.016 \pm 0.003$
15	0.190–0.227	$0.764 \pm 0.012 \pm 0.005$
16	0.227–0.275	$0.518 \pm 0.008 \pm 0.002$
17	0.275–0.337	$0.326 \pm 0.006 \pm 0.002$
18	0.337–0.418	$0.194 \pm 0.004 \pm 0.001$
19	0.418–0.523	$0.109 \pm 0.003 \pm 0.001$
bin	range	$1/\sigma \times (d\sigma/d\phi_\eta^*)(\times 100)$
20	0.523–0.657	$5.478 \pm 0.166 \pm 0.050$
21	0.657–0.827	$2.610 \pm 0.102 \pm 0.040$
22	0.827–1.041	$1.167 \pm 0.061 \pm 0.026$
23	1.041–1.309	$0.538 \pm 0.038 \pm 0.017$
24	1.309–1.640	$0.212 \pm 0.022 \pm 0.011$
25	1.640–2.049	$0.104 \pm 0.015 \pm 0.008$
26	2.049–2.547	$0.046 \pm 0.009 \pm 0.005$
27	2.547–3.151	$0.022 \pm 0.006 \pm 0.003$
28	3.151–3.878	$0.013 \pm 0.004 \pm 0.002$
29	3.878–4.749	$0.009 \pm 0.003 \pm 0.001$

TABLE III: Table of results for the dimuon channel for $|y| < 1$ region $30 < m_{\ell\ell} < 60$ GeV. The first quoted uncertainty is statistical and the second is the total experimental systematic uncertainty.

bin	ϕ_η^* range	$1/\sigma d\sigma/d\phi_\eta^*$
1	0.000–0.010	$7.87 \pm 0.14 \pm 0.12$
2	0.010–0.020	$7.25 \pm 0.13 \pm 0.12$
3	0.020–0.030	$6.98 \pm 0.13 \pm 0.09$
4	0.030–0.040	$6.36 \pm 0.12 \pm 0.06$
5	0.040–0.051	$5.68 \pm 0.11 \pm 0.05$
6	0.051–0.062	$5.15 \pm 0.10 \pm 0.03$
7	0.062–0.075	$4.70 \pm 0.09 \pm 0.03$
8	0.075–0.092	$3.98 \pm 0.08 \pm 0.02$
9	0.092–0.115	$3.21 \pm 0.06 \pm 0.03$
10	0.115–0.148	$2.32 \pm 0.04 \pm 0.03$
11	0.148–0.198	$1.65 \pm 0.03 \pm 0.02$
12	0.198–0.273	$0.98 \pm 0.02 \pm 0.01$
bin	range	$1/\sigma \times (d\sigma/d\phi_\eta^*)(\times 100)$
13	0.273–0.382	$52.61 \pm 1.07 \pm 0.73$
14	0.382–0.541	$25.07 \pm 0.63 \pm 0.35$
15	0.541–0.766	$11.88 \pm 0.36 \pm 0.18$
16	0.766–1.080	$5.05 \pm 0.21 \pm 0.11$
17	1.080–1.509	$2.36 \pm 0.12 \pm 0.07$
18	1.509–2.087	$1.17 \pm 0.08 \pm 0.06$
19	2.087–2.853	$0.40 \pm 0.04 \pm 0.03$
20	2.853–3.853	$0.19 \pm 0.02 \pm 0.02$

TABLE IV: Table of results for the dimuon channel for $1 < |y| < 2$ region $30 < m_{\ell\ell} < 60$ GeV. The first quoted uncertainty is statistical and the second is the total experimental systematic uncertainty.

bin	ϕ_η^* range	$1/\sigma \, d\sigma/d\phi_\eta^*$
1	0.000–0.010	$7.89 \pm 0.19 \pm 0.12$
2	0.010–0.020	$7.06 \pm 0.18 \pm 0.10$
3	0.020–0.030	$6.77 \pm 0.17 \pm 0.09$
4	0.030–0.040	$6.25 \pm 0.16 \pm 0.05$
5	0.040–0.051	$5.78 \pm 0.16 \pm 0.06$
6	0.051–0.062	$5.37 \pm 0.14 \pm 0.06$
7	0.062–0.075	$4.76 \pm 0.13 \pm 0.02$
8	0.075–0.092	$4.05 \pm 0.10 \pm 0.04$
9	0.092–0.115	$3.18 \pm 0.08 \pm 0.04$
10	0.115–0.148	$2.40 \pm 0.06 \pm 0.02$
11	0.148–0.198	$1.68 \pm 0.04 \pm 0.02$
12	0.198–0.273	$1.00 \pm 0.02 \pm 0.01$
bin	range	$1/\sigma \times (d\sigma/d\phi_\eta^*)(\times 100)$
13	0.273–0.382	$54.80 \pm 1.48 \pm 0.70$
14	0.382–0.541	$26.13 \pm 0.85 \pm 0.38$
15	0.541–0.766	$11.51 \pm 0.49 \pm 0.25$
16	0.766–1.080	$4.39 \pm 0.26 \pm 0.10$
17	1.080–1.509	$1.82 \pm 0.15 \pm 0.06$
18	1.509–2.087	$0.63 \pm 0.07 \pm 0.02$
19	2.087–2.853	$0.26 \pm 0.04 \pm 0.03$
20	2.853–3.853	$0.17 \pm 0.04 \pm 0.02$

TABLE V: Table of results for the dimuon channel for $160 < m_{\ell\ell} < 300$ GeV region. The first quoted uncertainty is statistical and the second is the total experimental systematic uncertainty.

bin	ϕ_η^* range	$1/\sigma \, d\sigma/d\phi_\eta^*$
1	0.000–0.010	$22.48 \pm 1.18 \pm 0.35$
2	0.010–0.020	$15.34 \pm 0.97 \pm 0.18$
3	0.020–0.030	$12.73 \pm 0.88 \pm 0.15$
4	0.030–0.040	$8.40 \pm 0.72 \pm 0.13$
5	0.040–0.051	$8.32 \pm 0.70 \pm 0.11$
6	0.051–0.062	$3.87 \pm 0.46 \pm 0.09$
7	0.062–0.075	$4.41 \pm 0.45 \pm 0.10$
8	0.075–0.092	$3.06 \pm 0.33 \pm 0.10$
9	0.092–0.115	$1.65 \pm 0.21 \pm 0.03$
10	0.115–0.148	$1.40 \pm 0.16 \pm 0.02$
11	0.148–0.198	$0.60 \pm 0.09 \pm 0.02$
bin	range	$(1/\sigma) \times (d\sigma/d\phi_\eta^*) \times 100$
12	0.198–0.273	$28.48 \pm 4.98 \pm 0.74$
13	0.273–0.382	$15.55 \pm 2.98 \pm 0.60$
14	0.382–0.541	$6.27 \pm 1.64 \pm 0.33$
15	0.541–0.766	$1.50 \pm 0.65 \pm 0.12$
16	0.766–1.080	$0.69 \pm 0.39 \pm 0.07$

TABLE VI: Table of results for the dimuon channel for $300 < m_{\ell\ell} < 500$ GeV region. The first quoted uncertainty is statistical and the second is the total experimental systematic uncertainty.

bin	ϕ_η^* range	$1/\sigma \, d\sigma/d\phi_\eta^*$
1	0.000–0.010	$28.17 \pm 3.93 \pm 0.57$
2	0.010–0.020	$22.38 \pm 3.40 \pm 0.34$
3	0.020–0.030	$18.70 \pm 3.06 \pm 0.41$
4	0.030–0.040	$6.61 \pm 1.80 \pm 0.18$
5	0.040–0.051	$4.76 \pm 1.48 \pm 0.10$
6	0.051–0.062	$3.14 \pm 1.16 \pm 0.12$
7	0.062–0.075	$1.91 \pm 0.84 \pm 0.14$
8	0.075–0.092	$2.11 \pm 0.78 \pm 0.06$
9	0.092–0.115	$1.40 \pm 0.53 \pm 0.06$
10	0.115–0.148	$0.68 \pm 0.30 \pm 0.12$
11	0.148–0.198	$0.54 \pm 0.22 \pm 0.04$
bin	range	$(1/\sigma) \times (d\sigma/d\phi_\eta^*) \times 100$
12	0.198–0.273	$2.98 \pm 5.47 \pm 0.21$
13	0.273–0.382	$7.78 \pm 4.95 \pm 0.47$
14	0.382–0.412	$2.24 \pm 2.57 \pm 0.20$